Local structure in ZrW_2O_8 from neutron total scattering

2007 J. Phys.: Condens. Matter 19 335215

(http://iopscience.iop.org/0953-8984/19/33/335215)

J. Phys.: Condens. Matter **19** (2007) 335215 (16pp) doi:10.1088/0953-8984/19/33/335215

Local structure in ZrW_2O_8 from neutron total scattering

Matthew G Tucker[1], David A Keen[1], John S O Evans[2] and Martin T Dove[3]

[1] ISIS Facility, Rutherford Appleton Laboratory, Chilton, Didcot, Oxon OX11 0QX, UK
[2] Department of Chemistry, University Science Laboratories, South Road, Durham DH1 3LE, UK
[3] Department of Earth Sciences, Cambridge University, Downing Street, Cambridge CB2 3EQ, UK

E-mail: d.a.keen@rl.ac.uk

Received 13 March 2007
Published 4 July 2007
Online at stacks.iop.org/JPhysCM/19/335215

Abstract

The local structure of the low-temperature ordered phase of the negative thermal expansion (NTE) material ZrW_2O_8 has been investigated by reverse Monte Carlo (RMC) modelling of neutron total scattering data. The local structure is described using the instantaneous distributions of bond lengths and angles obtained from the RMC-derived models which are simultaneously consistent with the average crystal structure. These results, together with their variation with temperature, show that the majority of the mean squared displacements of the atoms are accounted for by rigid unit mode (RUM) motions of the ZrO_6 octahedra and WO_4 tetrahedra. The detailed structural description presented in this paper further supports the dominance of the basic RUM interpretation of NTE in ZrW_2O_8 where rigid ZrO_6 and WO_4 polyhedra are joined by flexible Zr–O–W linkages.

(Some figures in this article are in colour only in the electronic version)

1. Introduction

Zirconium tungstate, ZrW_2O_8, is the archetypal isotropic negative thermal expansion (NTE) material [1, 2], with negative thermal expansion behaviour observed in a temperature range of over 1000 K and a large linear thermal expansion coefficient of -9.1×10^{-6} K^{-1} between 2 and 350 K [3]. The apparent simplicity of its cubic structure coupled with its significant NTE has led to a large literature on the underlying structural and dynamical origin of NTE in ZrW_2O_8 (see, for example, [4]).

The structure consists of a network of ZrO_6 octahedra and WO_4 tetrahedra, with each octahedron fully connected to six tetrahedra via the corner-sharing of oxygen atoms (see figure 1). The structure has the potential to be very flexible, with no edge or face-sharing structural units and a relatively low density ($\rho = 0.056\,88$ atoms Å^{-3} at 2 K). In addition,

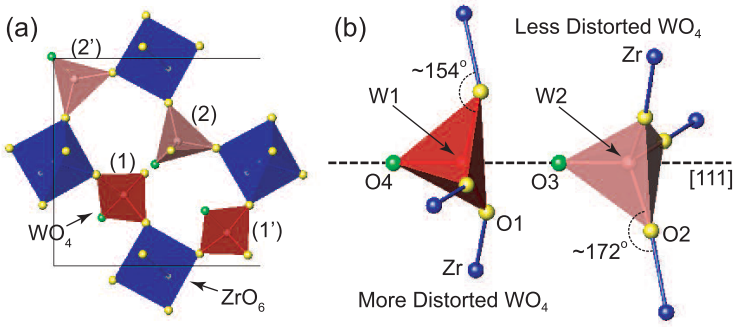

Figure 1. Schematic diagram of the structure of the low-temperature α-phase of ZrW_2O_8: (a) shows the arrangement of ZrO_6 octahedra and WO_4 tetrahedra; (b) gives further details of the environment around the unconnected WO_4 tetrahedral pairs and defines an atom labelling scheme consistent with [3].

although the ZrO_6 octahedra have no unconnected oxygen atoms, only three of the WO_4 tetrahedral oxygen atoms are joined to ZrO_6 octahedra. The relative orientation of the remaining non-bridging W–O bond within pairs of neighbouring, but unconnected, WO_4 tetrahedra and nearby WO_4 tetrahedral pairs gives rise to a further 'order–disorder' transition at 448 K. In the low-temperature α-phase the non-bridging W–O bonds of all WO_4 tetrahedral pairs align along the three-fold axes in space group $P2_13$. As the transition is approached from below, a significant number of WO_4 pairs begin to align in the opposite direction along the three-fold axes and above 448 K the alignment is random, with 50% of WO_4 pairs in each direction. The average high-temperature β-phase structure is then described using a split-site model within space group $Pa\bar{3}$ [3].

The so-called 'Rigid Unit Mode' (RUM) model has been successful in describing the dynamical origin of NTE in ZrW_2O_8 [5]. In the RUM model it is assumed that the local structural units can be treated as rigid bodies and the low-energy dynamics are dominated by their rotations and translations, facilitated by flexible corner-sharing linkages. This is an appropriate model if the energies required to distort the polyhedra are significantly larger than those required to rotate or translate them. It was found that the RUMs calculated from a 'split-atom' model of ZrW_2O_8 occurred on a complex three-dimensional surface in reciprocal space. In addition, four bands of low-energy 'quasi-RUMs' (qRUMs) were observed. The NTE in ZrW_2O_8 is ascribed to an increased amplitude of ZrO_6 octahedral and WO_4 tetrahedral rotation with increased temperature. This causes a broader distribution of W–O–Zr linkage angles and, as a result, the polyhedral centres approach each other more closely on average. Contraction occurs, because this is a larger effect than the thermal expansion of individual atomic bonds within the polyhedra.

The average structural description of ZrW_2O_8 obtained from Rietveld refinement of neutron diffraction data gives indications that this RUM model is plausible [3]. For example, anisotropic atom displacement parameters for the bridging oxygen atoms show large increases with increased temperature in directions which may be associated with increased librational amplitudes of the polyhedra, given that these are accompanied by minimal changes in intra-polyhedral bond angles. However, a measurement that is sensitive to local structure and local correlated deviations from the average structure would be expected to give a more convincing experimental validation of the dynamical RUM model for NTE. X-ray absorption spectroscopy (XAS) is one such measurement, where the fine structure above an absorption edge may be used to determine the local environment around the absorbing atom. Recent

XAFS measurements [6, 7] at the W L_{III} and Zr K edges have been interpreted in terms of a relatively stiff W–O–Zr linkage, in so far as the magnitude and variation with temperature of the standard deviation of the distribution of W–Zr interatomic distances obtained from the XAFS data is comparable with those of the Zr–O intra-octahedral distribution. Based on this observation, it was concluded that, at low temperatures, motions of the WO_4 tetrahedra and its three neighbouring ZrO_6 octahedra were correlated and the simple RUM model was inappropriate. Instead, vibrations between W–W and Zr–Zr atom pairs were invoked to explain NTE in ZrW_2O_8. A consequence of this interpretation, and in line with other more flexible models, is that the WO_4 tetrahedra translate significantly along $\langle 111 \rangle$ directions.

Another method which probes the local correlations in materials is total scattering. Data from total scattering may be Fourier transformed to give a weighted sum of partial pair correlation functions. This measurement is complementary to XAFS, in the sense that it is quantitative but not explicitly atom specific; XAFS is atom specific, but in some cases systematic errors may be introduced during the data treatment through corrections which are themselves dependent on the structure (see section 4). Recent developments of total scattering from crystalline materials using high real-space resolution time-of-flight neutron diffraction, combined with reverse Monte Carlo (RMC) modelling, have shown that, to a great extent, separation between partial pair distribution functions can be achieved effectively [8]. In addition, the RMC analysis produces a three-dimensional model of the structure which fits the total scattering data and Bragg intensities. Hence the local correlations extracted from this analysis are self-consistent (in the sense that they have been obtained from a three-dimensional representation of the structure) and are consistent with the average structure (the model agrees with the Bragg intensities).

In the light of the unexpected result from XAFS, a study of the local structure of the low-temperature α-phase of ZrW_2O_8 using total scattering has been carried out. Recent infrared spectroscopic results [9], which show a mixing of librational and translational character in the low-energy modes, provide further motivation for determining how the local structure disorders in response to the dynamical processes in ZrW_2O_8. An initial report, which gave an overview of the results, has already been published [10]. This current paper provides greater structural detail and, in particular, describes how the local structure responds to increases in temperature and hence enables the observed NTE. The rest of the paper is organized as follows: section 2 contains details of the experiment, data treatment, Rietveld refinement and RMC modelling. This is followed by a description of the results in terms of both the average and the local structure. These results are then compared with previously published diffraction and XAFS data and, based on this comparison, a conclusion is drawn about whether these data can be used to provide experimental support for the RUM picture of NTE in ZrW_2O_8.

2. Experimental details and RMC analysis

A 2 cm^3 sample of finely powdered ZrW_2O_8 was loaded into an 8 mm diameter thin-walled vanadium can and placed onto the cold finger of a closed-cycle helium refrigerator (CCR). This was mounted into the sample position of the GEM diffractometer at the ISIS spallation neutron source [11]. Diffraction data as a function of neutron time-of-flight were collected from the sample in three of the GEM detector banks centred at $2\theta = 17.98°, 63.62°$ and $91.30°$. Measurements were taken at 10, 100, 200 and 300 K for around 6 hours per temperature. Measurements of the empty can, empty CCR, empty instrument and an 8 mm diameter vanadium rod were also taken for background subtraction and data correction. The data were normalized using standard routines [12] to produce total scattering structure factors on an absolute scale and data suitable for Rietveld refinement.

The average structure was refined using the Rietveld method with multi-bank data and the GSAS refinement program [13]. In addition to the structural parameters, eight background parameters, an overall scale factor and two peak-shape parameters were refined for each of the three banks of data. RMC modelling, which has been described in detail elsewhere [8, 14], was then used to refine a $4 \times 4 \times 4$ supercell model of ZrW_2O_8, starting from the average structure determined from the Rietveld refinement results at each temperature. In brief, during each iteration of the RMC method, one randomly selected atom is randomly moved and a number of structural functions are recalculated from the model. If the difference between these calculated functions and the equivalent ones measured experimentally is improved, then the move is accepted; if the agreement is worsened, then the move is accepted with a certain probability. Iterations are continued until the calculated functions agree with the data within certain pre-defined limits and further iterations merely cause the agreement function to oscillate around an average value. Most of the results presented here are from an average over eight independent RMC models.

In this particular case, the RMC model was refined against the total scattering structure factor, $F(Q)$, the total pair distribution function, $D(r)$ and the powder pattern, $I(t)$, the last function measured using the detector bank centred on $2\theta = 63.62°$ and using the background, scale factor and peak-shape parameters from the Rietveld refinement. The definitions of $D(r)$, $F(Q)$ and the partial radial distribution functions, $g_{ij}(r)$, used later in this paper have been given previously [15]. Furthermore, to restrain the shape of the ZrO_6 octahedra and WO_4 tetrahedra and to maintain the network connectivity, the model was also refined against the Zr–O and W–O bond lengths and intra-octahedral and intra-tetrahedral bond angles, albeit with a low weighting. Hence the agreement function, χ^2_{RMC}, was defined as follows:

$$\chi^2_{\mathrm{RMC}} = \chi^2_{\mathrm{Data}} + \chi^2_{\mathrm{Restraints}} \tag{1}$$

where

$$\chi^2_{\mathrm{Data}} = \sum_k \sum_{i=1}^{n} \left[F_{\mathrm{calc}}(Q_i) - F_{\mathrm{exp}}(Q_i)\right]^2/\sigma(Q_i) + \sum_{i=1}^{m} \left[D_{\mathrm{calc}}(r_i) - D_{\mathrm{exp}}(r_i)\right]^2/\sigma(r_i) + \sum_{i=1}^{l} \left[I_{\mathrm{calc}}(t_i) - I_{\mathrm{exp}}(t_i)\right]^2/\sigma(t_i) \tag{2}$$

and

$$\chi^2_{\mathrm{Restraints}} = w_{\mathrm{Zr-O}} \sum_{\mathrm{Zr-O}} (r_{\mathrm{Zr-O}} - R_{\mathrm{Zr-O}})^2 + w_{\mathrm{O-Zr-O}} \sum_{\mathrm{oct}} (\theta_{\mathrm{O-Zr-O}} - \Theta_{\mathrm{O-Zr-O}})^2 + w_{\mathrm{W-O}} \sum_{\mathrm{W-O}} (r_{\mathrm{W-O}} - R_{\mathrm{W-O}})^2 + w_{\mathrm{O-W-O}} \sum_{\mathrm{tet}} (\theta_{\mathrm{O-W-O}} - \Theta_{\mathrm{O-W-O}})^2 \tag{3}$$

summing over the n data points in $F(Q)$ from each of the k detector banks, the m data points in $D(r)$, the l data points in $I(t)$, and all the M–O bonds and angles within the octahedra (M = Zr) and tetrahedra (M = W) in the model. $R_{\mathrm{M-O}}$ and $\Theta_{\mathrm{O-M-O}}$ are the mean intra-polyhedral M–O distances (obtained from the appropriate peaks in the real-space total pair distribution function at each temperature) and angles (90° and 109.47° for M = Zr and W, respectively). The σ and w parameters determine the relative weighting of the separate terms in equations (1)–(3) and were kept fixed throughout. Small values of $w_{\mathrm{M-O}}$ and $w_{\mathrm{O-M-O}}$ were chosen to ensure that the low-r M–O and O–O peaks in $D(r)$ were no sharper than those observed experimentally and to allow the distributions of intra-polyhedral distances and angles to reflect the experimental data rather than the restraints. These restraints also ensured that the topology of the network structure was preserved during RMC refinement.

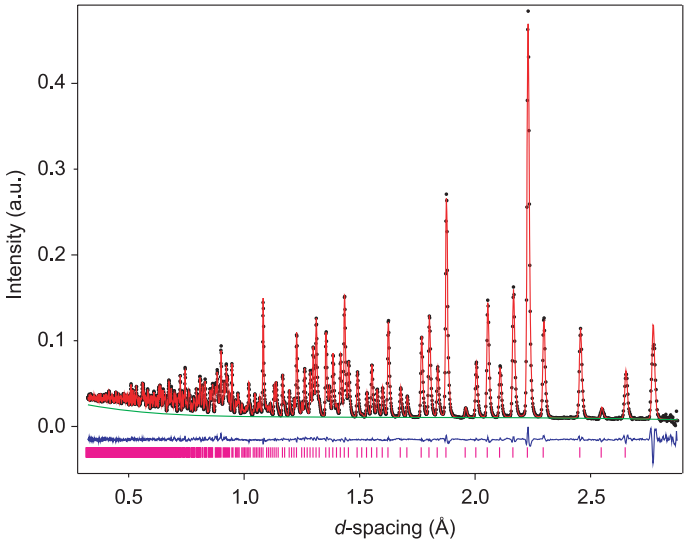

Figure 2. Powder pattern from ZrW_2O_8 at 10 K measured on the GEM diffractometer at ISIS. Data shown are from detectors centred at $2\theta = 91.30°$. Points, fitted and smooth lines show experimental data, Rietveld refined diffraction profile and background, respectively. The lower trace shows the difference and the vertical lines mark the positions of the expected Bragg peaks.

Table 1. Summary of the Rietveld refined structural parameters of ZrW_2O_8 at 10 K in space group $P2_13$ with cell parameter $a = 9.179\,40(2)$ Å. Atom labels refer to those given in figure 1.

	x in 4a(xxx) or xyz in 12b(xyz)			U_{iso} (Å^2)
Zr		0.001 17(8)		0.002 04(8)
W1		0.341 34(7)		0.000 89(19)
W2		0.599 98(7)		0.000 13(16)
O1	0.205 99(7)	0.439 76(8)	0.446 36(8)	0.003 9(1)
O2	0.786 47(7)	0.568 50(8)	0.554 86(8)	0.003 7(1)
O3		0.491 73(9)		0.005 8(2)
O4		0.233 05(6)		0.005 6(2)

3. Results

Representative Rietveld refined GEM data from ZrW_2O_8 are shown in figure 2. High-quality data were obtained at each temperature, enabling a precise determination of the average structure (see table 1). The refined structural parameters are consistent with previously reported values [3] although, since the main purpose of these refinements was to obtain starting models for subsequent RMC refinement, anisotropic displacement parameters were not used.

Similarly, good agreement with the experimental data was achieved from the RMC modelling (see figure 3). Figure 4 shows a picture of the RMC-generated model of ZrW_2O_8 at 10 K. The models were then investigated to determine 'instantaneous' bond length and bond angle distributions. Note that there is a difference between the bond lengths, or indeed any interatomic distances, deduced from a Rietveld refined structure and from a structural model based on total scattering data. The Rietveld refined structure is an average structure reflecting the elastic nature of Bragg scattering. Bond lengths determined in this way are therefore distances between the average positions of two atoms, i.e. ⟨A⟩–⟨B⟩, within the

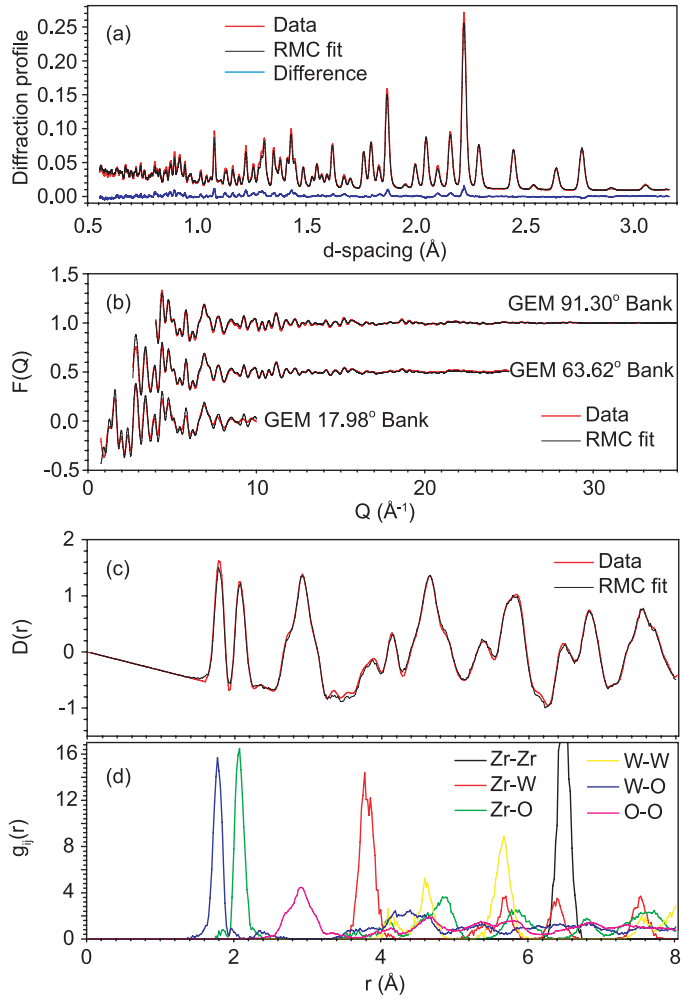

Figure 3. Comparison of experimental data and the equivalent functions calculated from the RMC model of ZrW_2O_8 at 10 K: (a) shows the RMC fit to the powder pattern from the GEM detector bank centred at $2\theta = 63.62°$; (b) shows the total structure factor, $F(Q)$, from the three GEM detector banks convoluted with the Fourier transform of a 'top-hat' function of size $2a$ to account for the finite size of the RMC model; and (c) and (d) show the low-r part of the total pair distribution function, $D(r)$, and the separate calculated partial $g_{ij}(r)$, respectively.

parameterization of the structural model. In contrast, total scattering is a measurement which contains scattering integrated over all neutron energy transfers with the sample, and models based on this measurement are snap-shots of the structure. These models give instantaneous separations between atom pairs. These may be averaged to yield 'instantaneous' bond lengths, namely ⟨A–B⟩. For short bonds these distances may also be obtained directly from the $D(r)$. These two definitions of bond lengths should produce very similar values for ordered crystals at low temperature, but when there is significant disorder, or correlated local motions, their values may be very different (see [16]). This is because reduced Bragg intensities at short d-spacings and anisotropic atomic displacement parameters, respectively, limit the sensitivity and the ability of a Rietveld refined model to represent a disordered structure reliably.

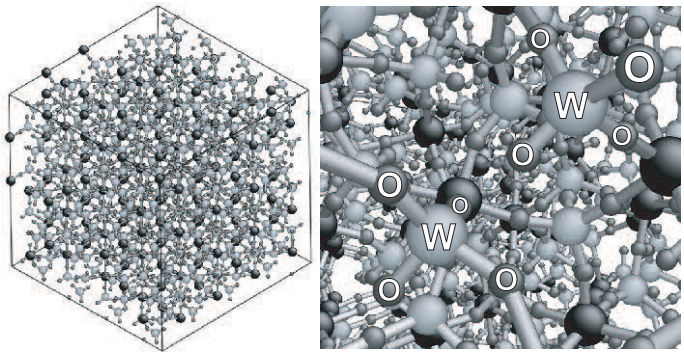

Figure 4. Two pictures of the RMC-generated model of ZrW_2O_8 at 10 K. The left-hand panel shows the complete $4 \times 4 \times 4$ supercell looking down a (111) direction and the right-hand panel is a detail of the same model showing a pair of WO_4 tetrahedra in the foreground. Zr, O and W atoms are shown as dark, mid- and light-grey spheres, respectively.

A similar argument can be made for bond angles determined from Bragg and total scattering. A key further benefit of importance to this study is that the distributions of bond lengths and angles can be determined directly from models based on total scattering. Models from RMC refinement of total scattering and Bragg intensities should reproduce local disorder within the 'constraint' of the average structure. They may therefore be used to calculate both ⟨A⟩–⟨B⟩ and the distribution of A−B bond lengths (including ⟨A–B⟩) and the equivalent bond angle distributions.

With this in mind, various bond lengths were presented in detail in [10] both from the Rietveld refined structure and the RMC structural model at 10 K. ⟨A⟩–⟨B⟩ distances were obtained from the RMC model by averaging the $4 \times 4 \times 4$ supercell onto one unit cell and calculating the distance between mean positions for each atom site within the unit cell. In contrast, ⟨A–B⟩ distances were obtained by calculating partial radial distribution functions, $g_{ij}(r)$, for a given atom pair within the RMC model and fitting the short distance peak (or peaks) with a Gaussian function (or functions). Hence the error on the pair distances is smaller than the standard deviation σ of the fitted Gaussian function. These partial radial distribution functions are calculated such that they distinguish between atoms of the same type that reside on different crystallographic sites, hence $g_{W1-Zr}(r)$ is different from $g_{W2-Zr}(r)$ etc. Indeed, any pair or angle correlation function may be calculated from the RMC model.

It was shown that there is little difference in the average short-range atom pair distances in ZrW_2O_8 at 10 K determined either by Rietveld refinement or from the RMC model (both ⟨A⟩–⟨B⟩ and ⟨A–B⟩) [10]. This indicates that the structure is ordered at low temperature and that the RMC model is a good representation of this ordered structure.

As pointed out recently [6, 7], the temperature dependence of σ^2 can be used to assess the relative stiffness of intra- and inter-polyhedral bonding. Representative Gaussian fits to the low-r peaks from a number of partial radial distribution functions are shown in figure 5 at the four measured temperatures. The $g_{W-W}(r)$ in the middle plot of figure 5 show two distinct distances; these correspond to the distance between tungsten atoms within WO_4 tetrahedral pairs ($W \cdots W_{pair}$; $W(1) \cdots W(2)$ in figure 1(a)) and the shortest distance via a ZrO_6 octahedron within the network; $W(1') \cdots W(2)$ in figure 1(a). All other $W \cdots W$ distances in the structure are ∼1 Å or more longer; for example, $W(1) \cdots W(1')$, $W(1) \cdots W(2')$ and $W(2) \cdots W(2')$ distances are all between 5.6 and 5.7 Å. As the temperature is increased, there is clear broadening and shifting (expansion or contraction) of these peaks.

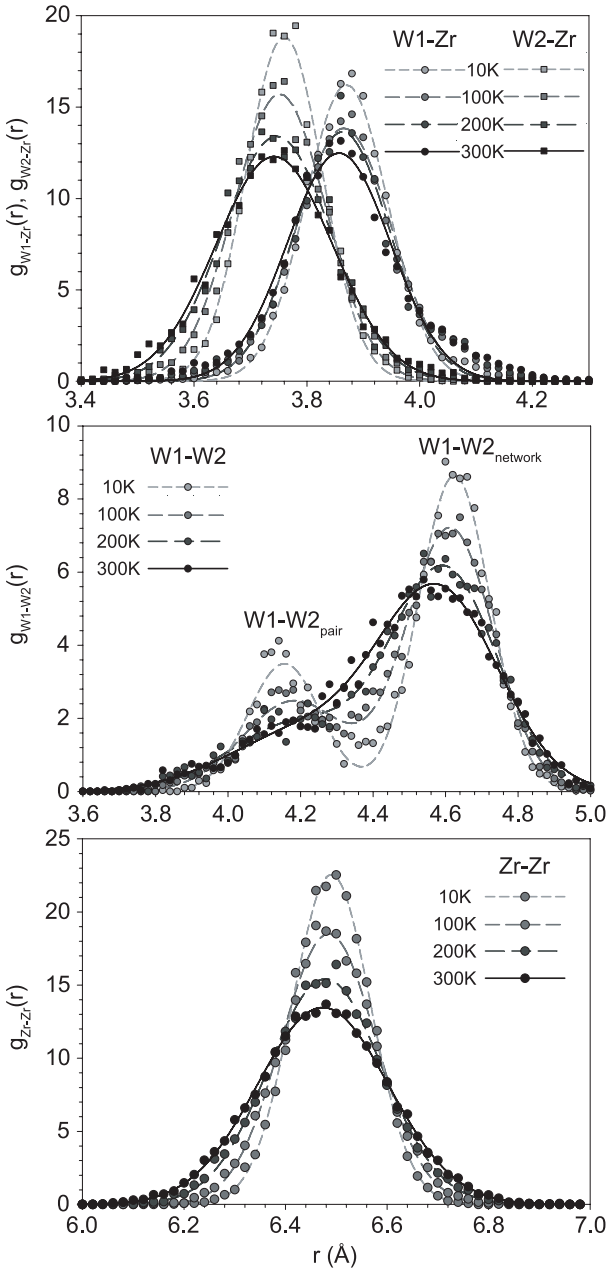

Figure 5. Plots showing low-r regions of partial radial distributions functions, $g_{ij}(r)$, (points) for W1 $\cdots$ Zr and W2 $\cdots$ Zr (upper plot, squares and circles, respectively), W1–W2 (middle plot) and Zr–Zr (lower plot) calculated from the RMC models of ZrW_2O_8 at 10, 100, 200 and 300 K. One or two Gaussian peaks (as appropriate) have been fitted to the data (smooth lines); although the Zr–Zr distribution contains two distances, only one Gaussian function has been fitted to this composite peak.

The Gaussian width parameters from the fits shown in figure 5 and from similar fitting of other partial radial distribution functions are shown in figure 6 at the four measured

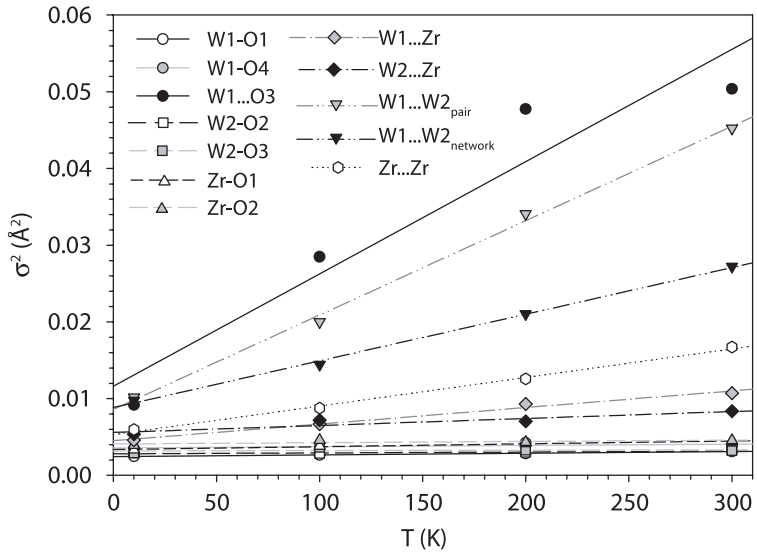

Figure 6. Plot showing fitted Gaussian width parameter σ^2 for a number of atom–atom distances in the RMC models of ZrW_2O_8 at different temperatures.

temperatures. The Zr–O and short W–O bonds are equally stiff, with a small change in σ^2 with temperature. In contrast, the indirect distances become increasingly flexible with increased temperature. For a network structure formed of flexibly linked rigid polyhedral units, one would expect that the temperature dependence of the width of a given atom pair distribution would be related to the number of links between the pair within the network. The slopes of the curves shown in figure 6 indicate that the atom pairs are ordered as follows (less flexible to more flexible): $Zr\cdots W2(1)$, $Zr\cdots W1(1)$, $Zr\cdots Zr(2)$, $W1\cdots W2_{network}(2)$, $W1\cdots W2_{pair}(4)$ and $W1\cdots O3(4)$, where the number in parentheses corresponds to the smallest number of W–O–Zr linkages between the atom pairs.

Further characterization of the flexibility of the Zr–O–W linkage is provided by the distribution of instantaneous bond angles within the RMC models. The representation of such functions should be carefully considered, since in three dimensions the number of angles available at angle θ is proportional to $\sin\theta$. It is therefore impossible to obtain a peak in the bond angle distribution function $B(\theta)$ at 180° (where $B(\theta)$ is the number of bonds between θ and $\theta + \Delta\theta$), even if a bond is fluctuating around this value. As a result, $B(\cos\theta)$ is sometimes shown, because the geometrical factor is constant for each $\Delta(\cos\theta)$ histogram even though $B(\cos\theta)$ distributions have reduced sensitivity near $\theta = 180°$. In this paper $B(\theta)/\sin\theta$ functions are shown [17]; these distributions accurately represent the bond angle probability whilst retaining sensitivity near 180°. Peaks in $B(\theta)/\sin\theta$ represent the most probable bond angles; mean bond angles may be different from these, especially near $\theta = 180°$. In order to achieve a suitable statistical accuracy near 180°, when the number of angles becomes vanishingly small, the distributions have been averaged from 100 independent RMC-generated configurations at each temperature.

$B_{Zr-O-W}(\theta)/\sin\theta$ are shown in figure 7. These distributions broaden significantly (see figure 8) with the peak in the distribution shifting slightly to lower (higher) angles with increased temperature for Zr–O1–W1 (Zr–O2–W2). The fitted Gaussian widths increase with temperature by $\sim$0.011° K^{-1} for both $B_{Zr-O-W}(\theta)/\sin\theta$ distributions. A much more

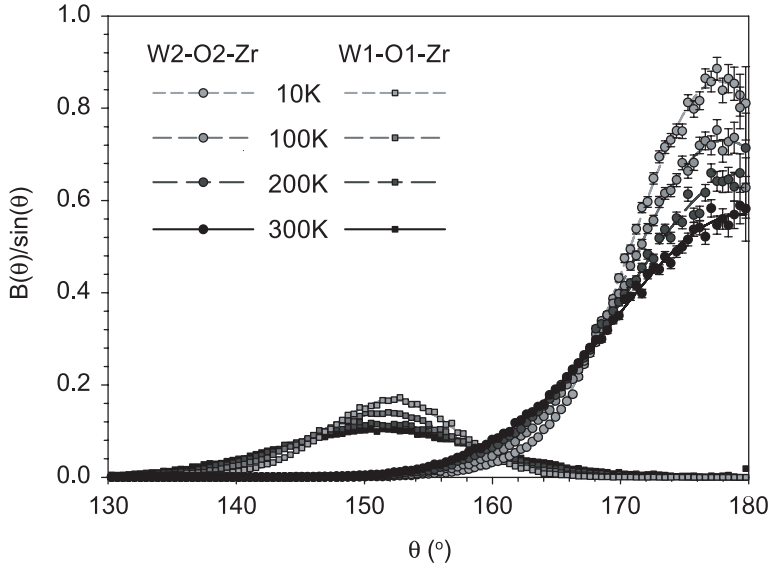

Figure 7. Plot showing the instantaneous bond angle distributions for Zr–O–W1 (squares) and Zr–O–W2 (circles) in ZrW_2O_8 at a number of temperatures. A Gaussian has been fitted to each set of data (lines).

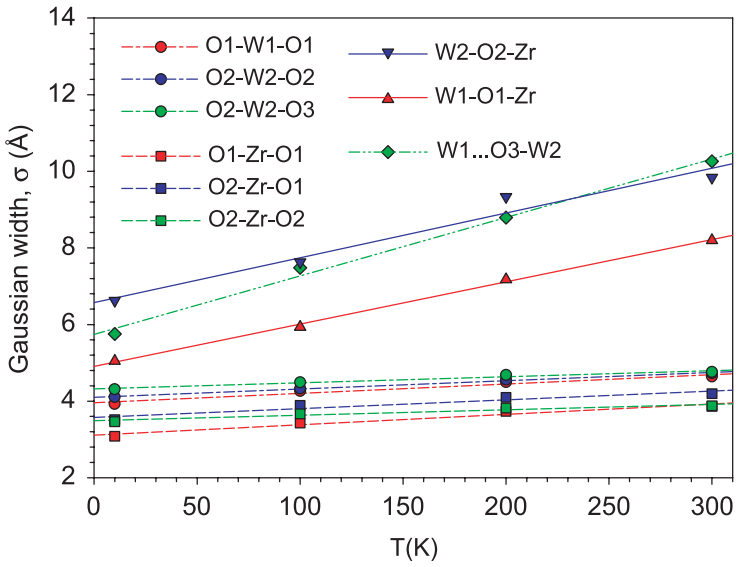

Figure 8. Plot showing the Gaussian width, σ, obtained from fitting the instantaneous bond angle distributions $B_{i-j-k}(\theta)/\sin\theta$ for O–Zr–O (squares), O–W–O (circles), W–O–Zr (triangles) and W1 $\cdots$ O3–W2 (diamonds) at a number of temperatures.

modest level of broadening is seen in the intra-polyhedral bond angle distributions (for example, the widths of $B_{O2-W2-O2}(\theta)/\sin\theta$ and the average $B_{O-Zr-O}(\theta)/\sin\theta$ only increase by $\sim 0.002^\circ\ K^{-1}$). This is a further indication that the polyhedra are more rigid than the linkages joining them. Figure 8 shows that the width of the W2–O2–Zr bond angle distribution is

Table 2. Summary of various average Zr–O–W bond angles (in degrees) of ZrW_2O_8 determined from RMC modelling ($\langle B_{W-O-Zr}(\theta)/\sin\theta\rangle$ and $\langle B_{W-O-Zr}(\theta)\rangle$) and Rietveld refinement. The Rietveld values are the angles between the positions of ⟨W⟩, ⟨O⟩ and ⟨Zr⟩ in the average structure. For a definition of the atom labels, see figure 1.

T (K)	$\langle B_{ijk}(\theta)/\sin\theta\rangle$	$\langle B_{ijk}(\theta)\rangle$	$\langle i\rangle-\langle j\rangle-\langle k\rangle_{\text{Rietveld}}$
		W1–O1–Zr	
10	152.1	151.5	154.4
100	151.3	150.4	154.5
200	151.3	149.7	154.0
300	151.2	149.3	154.5
		W2–O2–Zr	
10	177.7	172.5	172.4
100	178.2	171.5	172.1
200	179.9	170.5	171.0
300	179.5	169.5	171.5

larger than that of the W1–O1–Zr distribution for all temperatures; the $W(2)O_4$ tetrahedra have more freedom to move within the network than the $W(1)O_4$ tetrahedra, which is consistent with their more linear average W–O–Zr bond angle distributions (∼172° and ∼154° for W2–O–Zr and W1–O–Zr, respectively). The effect of thermal broadening on $B(\theta)$ distributions which peak above $\theta = 90°$ is to cause the average value to occur at lower θ. This is seen in both $B_{Zr-O-W}(\theta)$ distributions, where the peaks shift to slightly lower values with increasing temperature (see table 2). It is also interesting to note that the intra-polyhedral distances ($\langle W-O\rangle$ and $\langle Zr-O\rangle$) and angles ($\langle B_{O-W-O}(\theta)/\sin(\theta)\rangle$ and $\langle B_{O-Zr-O}(\theta)/\sin(\theta)\rangle$) show that the polyhedra become more regular as temperature increases.

4. Discussion

It is clear that the results presented in the previous section do not agree with the interpretation of the published XAFS data [6, 7], especially when considering the temperature dependence of the Gaussian width parameter, σ^2. Although this has already been discussed [10], three important differences are highlighted here:

(1) In general, the results from XAFS data yield smaller values of σ^2 than those from total scattering data.
(2) The XAFS results show similar temperature dependence for σ^2_{Zr-O} and $\sigma^2_{Zr\cdots W}$. In contrast these parameters, obtained from RMC analysis of total scattering data, have a different temperature dependence, and instead the behaviour of σ^2_{Zr-O} is more similar to the various bonded σ^2_{W-O}.
(3) The temperature dependence of $\sigma^2_{W1\cdots W2}$ for the two bonds is similar from the XAFS results, although $\sigma^2_{W1\cdots W2}$ values for the 'network' distance are higher than for the 'pair' distance; RMC analysis shows that $\sigma^2_{W1\cdots W2}$ for the 'pair' distance is much less stiff than for the 'network' distance.

The XAFS analysis is based on a fitting method which uses a 'theoretical standard' single peak for bonds which are too close together to be distinguished [7]. Therefore the separate W–O, Zr–O, Zr···W and Zr···Zr distances were grouped during the analysis. This would imply that σ^2 should be higher from XAFS than total scattering and not vice versa: indeed, it is

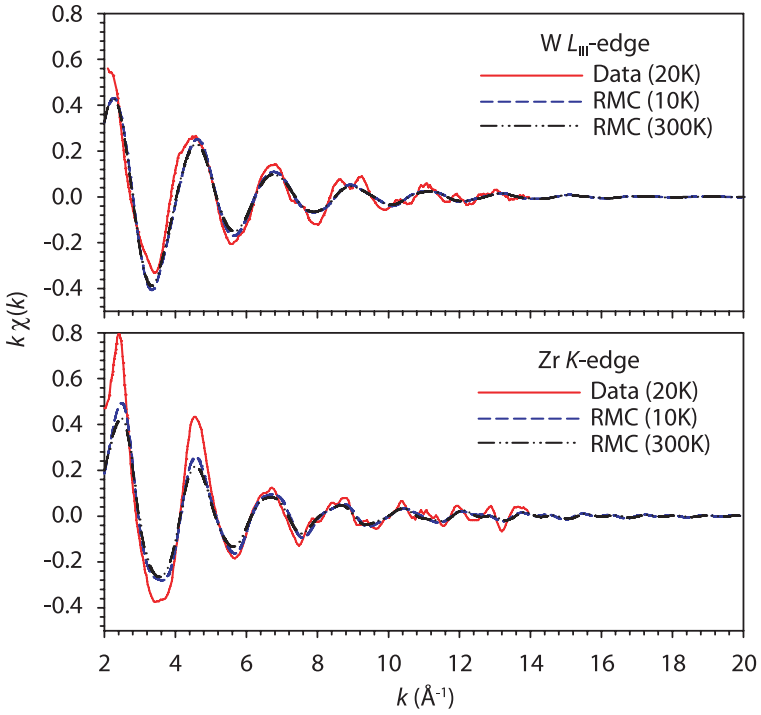

Figure 9. W L_{III}-edge (upper) and Zr K-edge (lower) XAFS data of ZrW_2O_8 at 20 K from Cao *et al* [7] (full line) compared with calculations from RMC models at 10 K (dashed line) and 300 K (dot dashed line).

curious that the XAFS $\sigma^2_{Zr\cdots W}$ implies a width which is smaller than the difference between the average distances for Zr · · · W1 and Zr · · · W2. In addition, many other atom pair distances are not incorporated in the XAFS fitting, especially W · · · O distances which overlap with the W · · · W distances above 4 Å. To counter this, the total scattering data do not obviously distinguish between distances which are very close together either, since all pair correlation distances are superimposed on each other. However, all distances are contained in the three-dimensional model and the individual distances may be extracted from the RMC model, because it is required to agree with the Bragg scattering which introduces a degree of directional separation (each Bragg peak is labelled with an *hkl* index). Furthermore, although the XAFS interpretation is based on data which separates pair correlations around Zr and W, the data contain strong multiple scattering terms which are very dependent on bond angle distributions. This is especially true for the Zr · · · W peak, where the overlapping multiple scattering terms are dependent on the Zr–O–W bond angle distribution [7]. The RMC results show that the Zr–O–W bond angle distributions are strongly temperature dependent (see figure 7), making this correction difficult to determine *a priori*.

It is possible to calculate the expected XAFS signal from the RMC models using the FEFF7 code [18]. Indeed, because the XAFS signal may be obtained using local clusters of instantaneous atom positions in the RMC model, it produces a representative result that bypasses the need for Debye Waller factors, theoretical standard distances, potentials or multiple scattering paths based on the average crystal structure. Figure 9 shows a comparison between the XAFS signal for the Zr K-edge and W L_{III}-edge (obtained by averaging over all Zr or W atom centres within a single configuration, respectively) calculated from the RMC

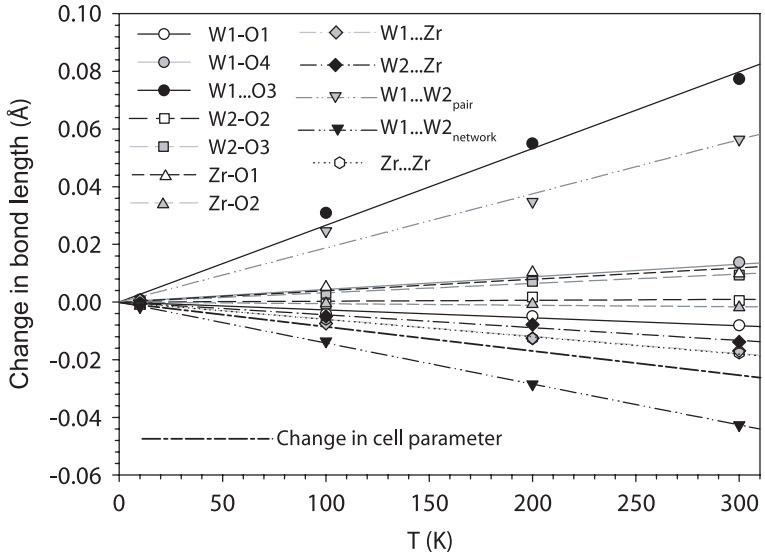

Figure 10. Plots showing the change in fitted peak distances ⟨A–B⟩ for a number of atom–atom distances in the RMC models of ZrW_2O_8 at a number of temperatures. The dot–dash–long dashed line shows the relative change in the cell parameter [3].

models at 10 and 300 K and the data of Cao *et al* [7] measured at 20 K. In general, there is good agreement between the calculation and the published data; the features are in phase, they decay at similar rates and have similar form. There are, however, some small differences, such as the double peaked feature at about 9 $Å^{-1}$ in the W L_{III}-edge data that is only calculated as a single peak from the RMC models. This high-frequency feature is likely to be due to multiple scattering rather than a signature of a structure with more order than the RMC model; indeed, our XAFS calculation from the ideal crystal structure only produced a slight asymmetry in this peak.

In view of the above discussion, there is sufficient uncertainty in the previous interpretation of the XAFS data to make it worthwhile pursuing the implications of the total scattering results on their own. Figure 10 shows the relative change in various atom–atom distances at a number of temperatures. The largest changes occur in the W1 · · · W2 distances, albeit in opposite senses. The W1 · · · W2 distance between the unlinked WO_4 tetrahedra pairs (together with the related W1 · · · O3 distance) expands, while the W1 · · · W2 shortest distance within the network contracts. The $W1 \cdots W2_{network}$ contraction is more than twice that of the other Zr · · · W and Zr · · · Zr network distances. This, taken with the minimal changes in W–O bond lengths, shows that the WO_4 tetrahedra move as rigid units and have the greatest 'freedom' within the structure. This is supported by geometrical analysis of the RMC configurations [10], which shows that a large component of the atomic motion is due to rigid-body rotations and translations; translations dominate rotations for the WO_4 tetrahedra, whereas rotations dominate translations for the ZrO_6 octahedra.

An expansion of the $W1 \cdots W2_{pair}$ distance with temperature is unexpected and this should be explored in more detail, particularly to try to understand how such a feature can contribute to NTE. The $W(1)O_4$, $W(2)O_4$ tetrahedral pairs in the structure are, on average, held too close to each other by the surrounding network. This is seen in the average Rietveld refined structure (cf figure 1) where (at 300 K) the W2–O2–Zr bond angle (171.5°) is more obtuse than the

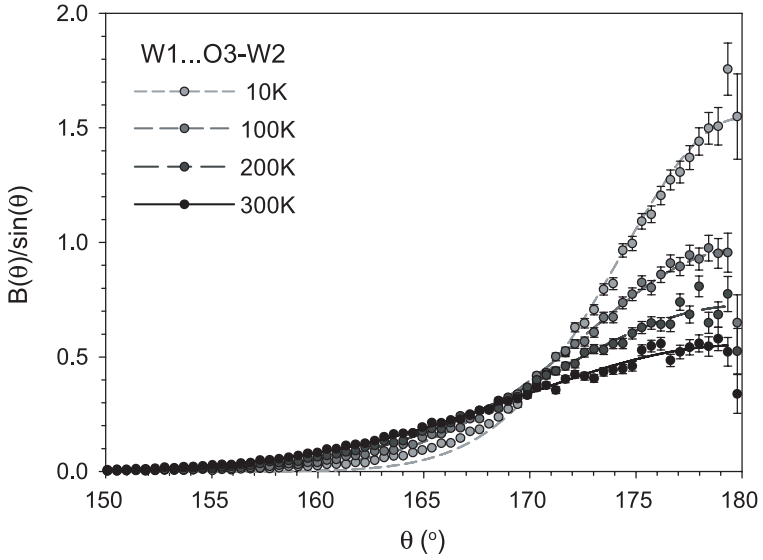

Figure 11. Plot showing the instantaneous bond angle distributions for W1 · · · O3–W2 at a number of temperatures (points) together with a Gaussian fit to each curve centred on $\theta = 180°$ (lines).

W1–O1–Zr bond angle (154.5°). This also affects the shape of the W(1)O_4 tetrahedra, which are distorted by the close proximity of the O3 atom (the O1 · · · O3 distance is 2.681 Å, the shortest O · · · O distance in the structure), with O1–W1–O1 and O4–W1–O1 bond angles of 115.9° and 101.8° and O1 · · · O1 and O1 · · · O4 distances of 3.078 and 2.744 Å, respectively. In contrast, the W(2)O_4 tetrahedra are largely undistorted, with O2–W2–O2 and O3–W2–O2 bond angles of 109.5° and 109.4° and O2 · · · O2 and O2 · · · O3 distances of 2.914 and 2.873 Å, respectively.

The average structure does not show these tetrahedra separating; indeed, they appear to move in phase with each other with the x-value of the (xxx) position of both W1 and W2 increasing at $\simeq 1.75 \times 10^{-6}$ K^{-1} (see supplementary information in [3]). This has led some to suggest that correlated translations of WO_4 tetrahedra along 111 directions are the dominant dynamical processes responsible for NTE. However, based on the change in the W x-parameters, the average positions of the WO_4 tetrahedra only move by $\simeq 0.001$ Å between 10 and 300 K. This is much smaller than the amount by which the W1 · · · $W2_{pair}$ distance (determined from the RMC-generated models) changes over the same temperature interval (see figure 10).

The instantaneous $\langle W1 \cdots W2 \rangle_{pair}$ distance may expand, while the average $\langle W1 \rangle \cdots \langle W2 \rangle_{pair}$ distance does not expand significantly if there is increased movement of WO_4 units perpendicular to the 111 direction joining the tetrahedral pairs. It is likely that these movements are accompanied by simultaneous rotations of the tetrahedra. Tetrahedral rotations will in turn cause Zr–O–W bond angle distributions to broaden and Zr · · · W distances to contract, especially where they are joined via near-linear Zr–O–W linkages. As a result of these tetrahedral movements, the W1 · · · O3–W2 bond angle distribution also broadens substantially with increased temperature, at a rate of 0.015° K^{-1} (see figures 11 and 8), whilst remaining peaked at 180°.

This in itself does not explain NTE; in fact, superficially quite the opposite! However, the effect of this local expansion of W1 · · · $W2_{pair}$, with its associated rotation, is to enable large

rotations of the ZrO_6 octahedra and to cause $W\cdots Zr$, $Zr\cdots Zr$ and, indeed, $W1\cdots W2_{network}$ distances to all decrease with temperature (see figure 10). These, being more rigidly associated with the macroscopic density, result in NTE. Furthermore, the increased separation of the WO_4 tetrahedral pairs causes the $W(1)O_4$ tetrahedra to become more regular, as seen, amongst others, in the larger-than-anticipated contraction of the longest W1–O1 bond with increased temperature (see figure 10). Simple bond valence arguments show that the polyhedral regularization provides an additional contribution to NTE, such that distortions should not be ignored in a full quantitative model.

The picture that emerges is of complex movements of WO_4 tetrahedra accompanied by complex movements of ZrO_6 octahedra. This is an important, experimentally derived conclusion, since it emphasizes that the NTE of ZrW_2O_8 is not driven by a simple mechanism based on a single low-energy vibrational mode, but rather that a combination of a large number of dynamical processes contribute collectively. This is consistent with the RUM/qRUM picture of ZrW_2O_8, where a large number of low-energy modes are distributed over a complex surface within the Brillouin zone [5], and in contrast to other simpler systems which only have a small number of RUMs limited to points, lines or high-symmetry planes in reciprocal space [19].

5. Conclusions

Total neutron scattering measurements analysed using the RMC modelling method have revealed the details of the local structure of ZrW_2O_8 at low temperature. The results show that NTE in this material occurs as a result of complex movement of loosely hinged corner-linked WO_4 tetrahedra and ZrO_6 octahedra, facilitated by the under-bonded WO_4 tetrahedra. There is no evidence for stiff Zr–O–W linkages found in recent XAFS measurements [6]. Hence the major contribution to NTE may be understood using a simple RUM model which predicts that a large number of low-energy modes will contribute to complex local behaviour and macroscopic volume reduction with increased temperature.

Acknowledgments

We are grateful to Daniel Bowron of the ISIS Facility for help in the interpretation of XAFS data. This work was funded, in part, by the UK's Engineering and Physical Sciences Research Council (EPSRC).

References

[1] Evans J S O, Mary T A, Vogt T, Subramanian M A and Sleight A W 1996 *Chem. Mater.* **8** 2809
[2] Mary T A, Evans J S O, Vogt T and Sleight A W 1996 *Science* **272** 90
[3] Evans J S O, David W I F and Sleight A W 1999 *Acta Crystallogr.* B **55** 333
[4] Barrera G D, Brunno J A O, Barron T H K and Allen N L 2005 *J. Phys.: Condens. Matter* **17** R217
[5] Pryde A K A, Hammonds K D, Dove M T, Heine V, Gale J D and Warren M C 1996 *J. Phys.: Condens. Matter* **8** 10973
[6] Cao D, Bridges F, Kowach G R and Ramirez A P 2002 *Phys. Rev. Lett.* **89** 215902
[7] Cao D, Bridges F, Kowach G R and Ramirez A P 2003 *Phys. Rev.* B **68** 014303
[8] Keen D A, Tucker M G and Dove M T 2005 *J. Phys.: Condens. Matter* **17** S15–22
[9] Hancock J N, Turpen C, Schlesinger Z, Kowach G R and Ramirez A P 2004 *Phys. Rev. Lett.* **93** 225501
[10] Tucker M G, Goodwin A L, Dove M T, Keen D A, Wells S A and Evans J S O 2005 *Phys. Rev. Lett.* **95** 255501
[11] Williams W G, Ibberson R M, Day P and Enderby J E 1998 *Physica* B **241–243** 234
Day P, Enderby J E, Williams W G, Chapon L C, Hannon A C, Radaelli P G and Soper A K 2004 *Neutron News* **15** 19
Hannon A C 2005 *Nucl. Instrum. Methods* A **551** 88

[12] Hannon A C, Howells W S and Soper A K 1990 *IOP Conf. Ser.* **107** 193
[13] Larson A C and von Dreele R B 2000 *Los Alamos Nat. Lab. Report* 86-748 unpublished
[14] McGreevy R L 2001 *J. Phys.: Condens. Matter* **13** R877
[15] Keen D A 2001 *J. Appl. Crystallogr.* **34** 172
[16] Dove M T, Tucker M G and Keen D A 2002 *Eur. J. Mineral.* **14** 331
[17] Ciunik Z and Desiraju G R 2001 *Chem. Commun.* **2001** 703
[18] Zabinsky S I, Rehr J J, Ankudinov A, Albers R C and Eller M J 1995 *Phys. Rev.* B **52** 2995
[19] Giddy A P, Dove M T, Pawley G S and Heine V 1993 *Acta Crystallogr.* A **49** 697